

Large Splitting Massive Schrödinger Kittens

Ryan J. Marshman,¹ Anupam Mazumdar,² Ron Folman,³ and Sougato Bose¹

¹*Department of Physics and Astronomy, University College London, Gower Street, WC1E 6BT London, United Kingdom.*

²*Van Swinderen Institute, University of Groningen, 9747 AG Groningen, The Netherlands.*

³*Department of Physics, Ben-Gurion University of the Negev, Be'er Sheva 84105, Israel.*

(Dated: March 6, 2022)

Probing quantum mechanics, quantum aspects of general relativity along with the sensing and the constraining of classical gravity can all be enabled by unprecedented spatial sizes of superpositions of massive objects. In this paper, we show that there is a feasible setup sourced by realisable magnetic field gradients $\mathcal{O}(10 - 100) \text{ Tm}^{-1}$ to construct a large spatial superposition of $\mathcal{O}(10^{-4} - 10^{-8}) \text{ m}$ for masses $\mathcal{O}(10^{-17} - 10^{-14}) \text{ kg}$ over a time period of up to 0.1 – 10 seconds.

At a microscopic level, three of the known forces of nature, electromagnetic (EM), weak and strong, obey the principles of quantum mechanics (QM) and local quantum field theory (QFT) [1]. However, the origin of gravitational attraction between two masses remains obscure at a microscopic level. There is no experimental proof yet of how the gravitational interaction is being mediated. Recently, a tabletop experiment has been suggested to explore the quantum origin of gravity in a tabletop experiment [2–4]. The protocol crucially relies on the interaction of quantum matter with quantum gravity, leading to the generation of entanglement between spins embedded in two non-relativistic test masses [3] as long as they are initially prepared in a quantum superposition of distinct spatial states. The spin entanglement witness will prove the graviton’s quantum-ness as a mediator of the force between the two masses (quantumness of the linearized metric fluctuations around a Minkowski background), and will further serve as a test bed of the nature of gravitational interaction at microscopic distances [3, 5]. A large splitting superposition of distinct spatially localised states of large masses is of immense practical interest in quantum sensing of weak forces, even enabling a tabletop detection of low-frequency gravitational waves, the quantum sensing of curvature, and frame-dragging [6].

Despite the clear importance of realising a quantum test of gravity, there remains a very demanding requirement: quantum spatial superpositions of neutral mesoscopic masses $m \sim 10^{-15} \text{ kg}$ over spatial separations of $\Delta x \sim 10 \mu\text{m}$ [7] far beyond the scales achieved to date (e.g., macromolecules $m \sim 10^{-22} \text{ kg}$ over $\Delta x \sim 0.25 \mu\text{m}$, or atoms $m \sim 10^{-25} \text{ kg}$ over $\Delta x \sim 0.5 \text{ m}$) [8, 9].

Beyond the usage in sensing quantum and classical gravity, upgrading the mass m and the superposition Δx , naturally stretches the boundaries of the validity of QM, which in itself is a worthy goal. However, there is a gap in the literature at the moment as far as a realistic scheme for achieving superposition sizes $\Delta x \gg 1 \mu\text{m}$ with nano-scale and micro-scale masses is concerned. While there are quite a few schemes for a lower Δx , or m , investigated at various levels of detail [10–30], and while these may suffice to falsify various purported modifications of

QM [31–33], the only two predictions stemming from the straightforward application of QM (local QFT to be more precise [3]) which would give us non-trivial information (e.g. sensing the quantum nature of gravity [2] and sensing extremely weak classical gravity [6]), necessarily seem to require $\Delta x \gtrsim 1 \mu\text{m}$.

Rudimentary arguments on how to achieve such superpositions using the Stern-Gerlach effect in very high magnetic field gradients were presented in the original proposal [2], building on some earlier ideas for smaller $m, \Delta x$ superpositions [18, 34]. A feasibility study building on atomic experiments was recently performed, showing that such a Stern-Gerlach Interferometer (SGI) for massive objects is indeed possible [29]. We now go further in several respects: First, we require more moderate magnetic gradients. Second, we take into account gradients in other directions, as demanded by Maxwell equations. Third, we take into account the diamagnetic forces, and, fourth, we consider a magnetic source which enables constant gradients over a large volume.

In the following we show that for entirely reasonable magnetic fields and moderate values of the magnetic field gradients, we can use a modified version of the SGI to generate the superpositions of nano and micron-scale masses with $\Delta x \gtrsim 1 \mu\text{m}$. Our work will closely follow the protocol of SGI, which has previously been experimentally demonstrated with atoms [29, 35–37]. In contrast to previous results [27], we will show how to avoid Majorana spin flips which is necessary to maintain the coherence of the spin during the experiment. We will argue that by using a gradient-free spatial region in which the diamagnetic force does not act, in conjunction with altered initial conditions, we can improve the splitting mechanism. These features allow us to present in detail a feasible interferometric accelerator for micro-scale masses, and enable the creation of a massive Schrödinger’s cat.

Previous experimental configurations considers a magnetic field which originates in a single current-carrying wire or a permanent magnet, whereby the field goes as $\vec{B} \propto 1/r$, where r is the distance from the source. The magnetic field can then be linearised in a small region within which it has an approximately constant magnetic

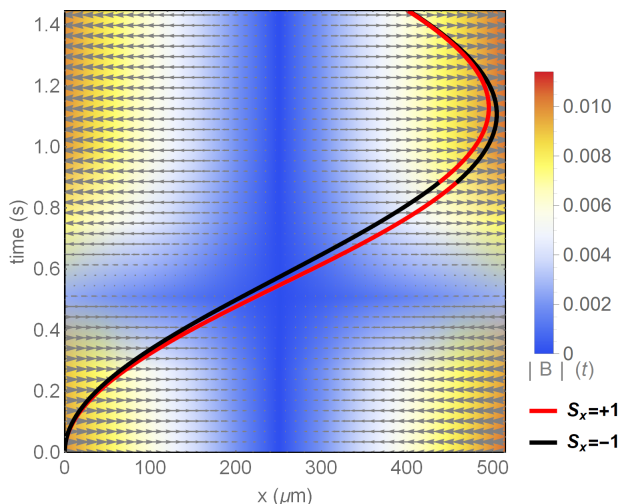


FIG. 1: Example interferometer path trajectories through the varying magnetic fields used. The magnetic field transition time here is accentuated for readability. Note that the internal spin states are reversed at time $t \approx 0.9$ s to ensure the interferometer is closed.

field gradient. However, a significant splitting will require long evolution times, and as a significant distance quickly develops between the particle and the wire, significant magnetic gradients are no longer available. We will therefore consider a configuration which enables a constant gradient over a large region (e.g. quadrupole field from coils in an anti-Helmholtz configuration). A typical resultant trajectory of such a potential is shown in Figure 1. We also take into account the limitations imposed by ensuring the magnetic field is physical and the associated limitations due to the low field dynamics of an electronic spin state.

Model: We assume a host crystal of micron dimensions with a single spin embedded in it, and concentrate, in this work, only on the translational motion of this crystal under an inhomogeneous magnetic field gradient. To explicitly model the spin and the host crystal material, we will assume a nitrogen-vacancy (NV) centre spin in a diamond nano/micro-crystal, although our results and analysis will hold for almost all materials which have similar values of diamagnetic susceptibility and generic electronic spins. The internal spin state due to the NV centre will be initialised in the state $\frac{1}{\sqrt{2}}(|1\rangle + |-1\rangle)$.

We consider the mass to be in a *free fall* along the z -axis. We do not therefore treat its motion along the z axis explicitly, which in our setting always commutes with the motion along the other two axes. Moreover, z motion would be absent in a drop-tower experiment, for example, which may be necessary in such experiments because of their long durations of ~ 1 s, and to mitigate the effect of any gravitational jitter experienced by the interferometer, which could induce unknown phases, see [38]. Under

this setting, we will realize a 1-dimensional SGI which, as time progresses, achieves first a maximum wavefunction splitting Δx in the x direction, and then its subsequent recombination to complete the interferometry. The external magnetic field \vec{B} varies in the $x - y$ plane, and as we will see, with our choice of its profile, couples predominantly to the x motion via the x -component of the spin. The Hamiltonian of the system is given by [27, 39]

$$H = \frac{\hat{P}_x^2 + \hat{P}_y^2 + \hat{P}_z^2}{2m} + mg\hat{z} + \hbar D \hat{S}_x^2 - \frac{\chi_m m}{2\mu_0} \vec{B}^2 - \mu_B \hat{s} \cdot \vec{B}, \quad (1)$$

where m is the mass of the diamond, $\chi_m = 6.2 \times 10^{-9} \text{ m}^3 \text{ kg}^{-1}$ is the mass magnetic susceptibility, μ_B is the Bohr magneton, \hat{s} is the spin operator, and $D = (2\pi) \times 2.8 \text{ GHz}$ is the NV zero-field splitting. Note that in writing the above Hamiltonian, we are only concentrating on the *translational motion* – we are assuming that the torque and the rotational effects of the mass can be made negligible.

There are known predicaments for generating superpositions by using a spin coupled to an external magnetic field. These are related to; (1) the electronic spin will in general experience Majorana spin-flip transitions, thus no longer remaining in a well-defined eigenstates as required for the coherent manipulation of the masses whenever the magnetic field magnitude becomes small, and (2) the effect of off-axis magnetic field gradients, which are generally not considered [27], however, this *must* be taken into account to satisfy Maxwell's equations.

First, we will consider the constraints on the magnetic field and seek to address these problems directly. Noting that $\vec{\nabla} \cdot \vec{B} = 0$ and $\vec{\nabla} \times \vec{B} = 0$, as we seek to ensure the mass is kept away from the source which creates the magnetic field. For simplicity, we may assume the following profile in the (x, y) plane: $\vec{B} = B_x(x, y)\hat{x} + B_y(x, y)\hat{y}$. We take the x axis as the *desired superposition direction*, and we require the magnetic field to be linear along x direction, with a constant magnetic field gradient along the x direction to take some constant value ∂B . To ensure that we can take the x -axis as our quantisation axis, and that Majorana spin flips are avoided, we require that $|B_x(x, y)| \gg |B_y(x, y)| \forall x, y$ in the vicinity of the controlled trajectories. The simplest general form for the magnetic field which will satisfy all the above conditions can be given by:

$$\vec{B}(x, y) = (B_x(0, 0) - \partial B x)\hat{x} + \partial B y \hat{y}, \quad (2)$$

for any fixed value of the magnetic field at the origin $B_x(0, 0)$ and magnetic field gradient ∂B . Note that for positive $B_x(0, 0)$ and ∂B the zero point of the magnetic field is always on the positive x axis. By ensuring that $y \approx 0$ during the entire interferometry, we can note that a suitable definition for the zero magnetic field region

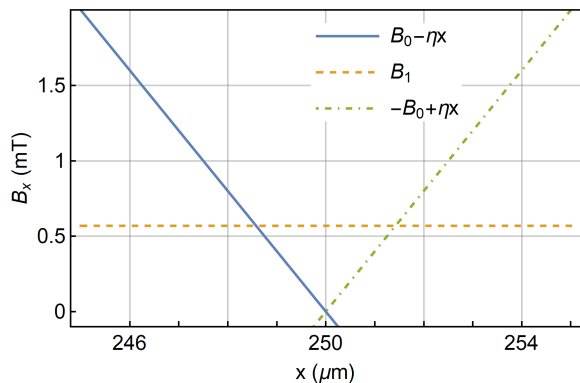


FIG. 2: Diagram of the x components of the magnetic fields considered. The inset figure shows detail around the zero-field region. The magnetic fields shown here were used for the $\eta = 40 \text{ Tm}^{-1}$ computation below with $B_0 = 10^{-2} \text{ T}$, $\eta = 40 \text{ Tm}^{-1}$ and $B_1 = 100\varepsilon \text{ T}$.

which must be avoided is

$$x \notin \left[\frac{B_x(0,0) - \varepsilon}{\partial B}, \frac{B_x(0,0) + \varepsilon}{\partial B} \right], \quad (3)$$

where ε is the minimum allowable magnetic field in the x direction. For a sufficiently large ε , we can ascertain that the spin states will always be approximately aligned in the quantisation axis in the x direction and Majorana spin flips are avoided.

The spin state in the y and z basis will experience a rapid Larmor precession, with a frequency set by $\omega_L = \frac{ge}{2m_e} |B(x,y)|$, where $g \approx 2$ is here the Landé g factor, e is the electron charge and m_e is the electron mass. If we desire a minimum Larmor frequency of ω_L^{min} , we can define a minimum allowable magnetic field magnitude:

$$\varepsilon \sim \frac{2m_e \omega_L^{\text{min}}}{ge}. \quad (4)$$

Therefore, the particle must not enter the region given by Eq.(3). To achieve this, we will use three linear magnetic field profiles sequentially in time, which are specific solutions of the form of equation 2:

$$\vec{B}(x,y) = (B_0 - \eta x) \hat{x} + \eta y \hat{y} \quad (5)$$

$$\vec{B}(x,y) = B_1 \hat{x} \quad (6)$$

$$\vec{B}(x,y) = -(B_0 - \eta x) \hat{x} - \eta y \hat{y} \quad (7)$$

with $B_0, B_1, \eta > 0$ as seen in Fig. 2. We then require $B_1 \gg \varepsilon$, and the timing of the switching between the magnetic fields will be done to ensure that the particle never experiences a small magnetic field. That is, as the particle approaches the disallowed region given by Eq. 3 (for $B_x(0,0) = B_0$ and $\partial B = \eta$), the magnetic field is mapped to that given by Eq. 6 (where now $B_x(0,0) = B_1$ and $\partial B = 0$, thus the region specified by equation 3 does not occur), and as it leaves that region, the magnetic field

is smoothly mapped to Eq. 7 (where $B_x(0,0) = -B_0$ and $\partial B = -\eta$). The switching function will be modelled by:

$$\text{Sw}(t, t_{on}, t_{off}) = 0.5 (\tanh[\delta(t - t_{on})] + 1) + 0.5 (\tanh[\delta(t_{off} - t)] + 1) \quad (8)$$

where δ is the switching frequency parameter, which we ensure to be sufficiently slow such that the magnetic field change is always adiabatic. This is to ensure that it does not complicate the spin dynamics. We consider $\delta = 10^3 \text{ Hz}$, which is well below what is required to maintain the adiabaticity conditions $\dot{\omega}_L/\omega_L^2 \ll 1$ and $\delta \ll \omega_L^{\text{min}}$. With this, since the magnetic field is along a fixed direction, it effectively freezes the spin direction (with the other spin components experiencing high-frequency Larmor precession).

Away from the nearly zero-field region, where the magnetic field profile is given by Eq.5 or 7, we can write the potential energy in a compact form as:

$$U_{\pm}(\tilde{x}') = -\frac{\chi_m m}{2\mu_0} \eta^2 \tilde{x}'^2 + \mu_{\pm} \frac{\mu_0}{\chi_m m} \quad (9)$$

where we have taken $y \approx 0$, while the second term is a constant energy, and $\tilde{x}' = x - C(s_x)$. The value of $C(s_x)$ is fixed by the internal spin state, s_x , and its interaction with the magnetic field gradient throughout the dynamics. The values $C(s_x)$ will take are

$$C(s_x = \pm 1) = B_0/\eta - \frac{ge\hbar}{2m_e \chi_m m \tilde{\eta}(t)} \mu_0, \quad (10)$$

where $\tilde{\eta}(t) = \eta$ when $t < \tau_1$ and $\tilde{\eta}(t) = -\eta$ when $t > \tau_4$. Thus the object sees a harmonic potential created by the diamagnetic interaction whose centre is displaced in the x direction by the spin-magnetic field gradient interaction. In Fig.3, we have shown on the harmonic oscillator potentials of two spin eigenstates. It is clear from the above that the object will roll in different potential wells corresponding to its spin state and thereby develop a momentum difference as they approach the nearly zero field region. It is in this region that we switch the gradient (the harmonic potential) off, and let the object evolve in a magnetic field given by Eq.(6) so that a continually increasing spatial splitting can develop due to the momentum difference of the spin components. This stage makes the key difference between this current set-up, and proposals of the qualitative form of Ref.[27] where a harmonic confinement is omnipresent. In our case, if the harmonic potential was always present, then the momentum difference would have started to become reduced immediately as the object reaches the centre of the well. Furthermore the added complexity of the spin dynamics due to Majorana spin flips should also be taken into account. However, in our case, the central region is replaced by a gradient-free central region (no harmonic potential region) in which the momentum difference can work to enhance the spatial splitting.

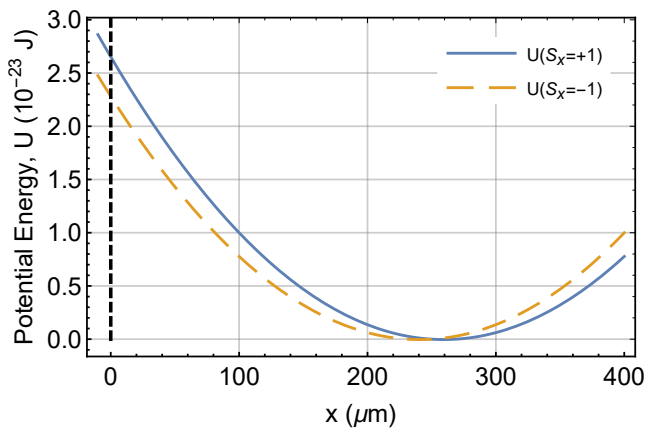


FIG. 3: Potential energy corresponding to both spin $S_x = +1$ and $S_x = -1$ for a magnetic field as given by Eq. 5. The initial position is shown by the vertical black dashed line.

The motion of the particle can be separated into different phases, largely depending on the form of \vec{B} :

1. $t < \tau_1$, \vec{B} is given by Eq.5, see blue line in Fig.2.
2. $\tau_1 \leq t < \tau_2$, \vec{B} is switching adiabatically from Eq.5 to Eq.6, via the switching function given by Eq.8.
3. $\tau_2 \leq t < \tau_3$, \vec{B} is given by Eq.6, see orange dotted line in Fig.2.
4. $\tau_3 \leq t < \tau_4$, \vec{B} is switching adiabatically from Eq.6 to Eq.7 via the switching function given by Eq.8.
5. $\tau_4 \leq t$, \vec{B} is given by Eq.7, see dotted-dashed green line in Fig.2.
6. $t = \tau_5$, when the spin states are reversed to close the superposition while \vec{B} is still given by Eq.7.
7. $t = \tau_6$, when the two wavefunctions are brought to overlap in the position and the momentum basis.

When the masses are in a coherent state of the harmonic potential, the wavefunction will hardly spread during the entire evolution due to the largeness of the mass. Thus, it is sufficient to consider that the centre of mass is following a classical trajectory. Thermal fluctuations in the initial state do not limit the coherence in the final state as they factor out of the motion, see for the discussions in [10, 18]. To a very good approximation, the two paths can be modelled by:

$$x(t) = A \cos(\omega t + \phi) + C(s_x) \quad (11)$$

This leaves the amplitude A and the phase ϕ to be determined by a set of initial conditions (discussed below and in the Appendix), specifically by requiring that the position and the momentum of each arm of the interferometer

are continuous throughout the trajectory. The frequency of the diamagnetic trap is given by $\omega = (-\chi_m/\mu_0)^{1/2}\eta$, while note that $\chi_m < 0$ as the mass is diamagnetic and so the frequency is real.

For the ease of computation, we have solved the complete trajectory for the two wave packets as an appropriate mixture of both analytic and numerical solutions to the equations of motion. For periods of evolution by a time independent Hamiltonian (essentially harmonic evolution), analytic solutions is used. However to allow for a more realistic magnetic field switching to be modelled, numerics are used, specifically during $\tau_1 \leq t < \tau_2$ and $\tau_3 \leq t < \tau_4$. This is discussed in more detail in the Appendix. The resulting motion can be seen in Figs.4a and 4b.

Note that at $\tau_5 \approx 0.9$ s (marked by the vertical line in Figs.4a and 4b), the spin reversal takes place by firing a rapid microwave pulse to alter the internal spin state. We can find numerically the final time τ_6 to be

$$\tau_6 \approx 59 \times (1 \text{ Tm}^{-1}/\eta) \text{ sec}, \quad (12)$$

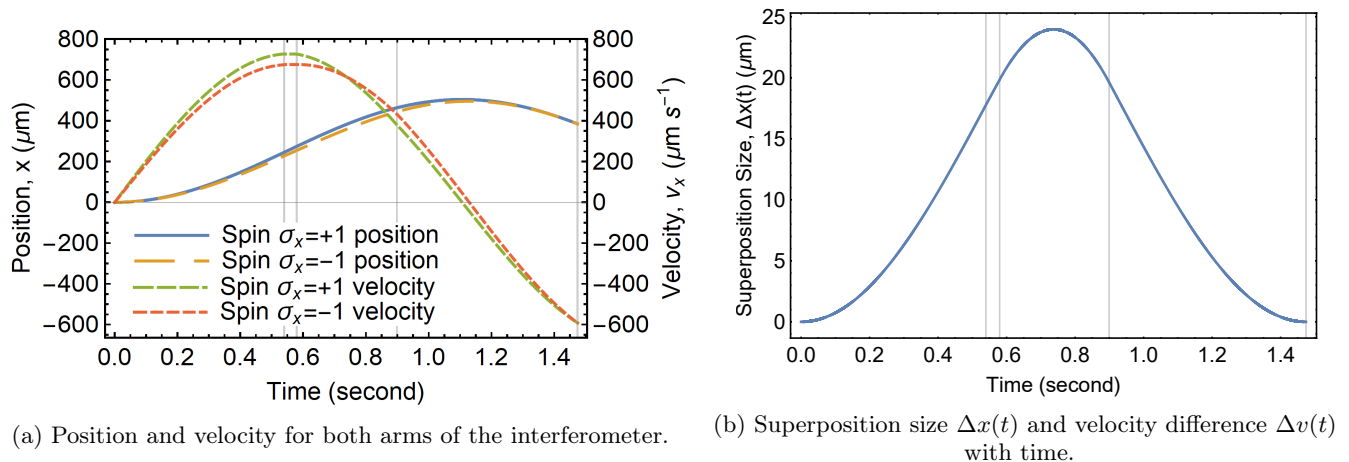
to ensure that the relative positions of the two paths $\Delta x(t = \tau_6) \approx 0$ m, and the relative velocity $\Delta v(t = \tau_6) \approx 0$ ms⁻¹.

This results in the superposition sizes as seen in Fig.5, and the trajectories through the interferometer can be seen as in Fig.4. Furthermore, the maximum superposition which occurs between $\tau_4 < t < \tau_5$ can be determined numerically:

$$\Delta x_{\max}(m, \tau_6) \approx \left(\frac{1.6 \times 10^{-16} \text{ Kg}}{m} \right) \left(\frac{\tau_6}{1 \text{ sec}} \right) \times 10^{-6} \text{ m} \quad (13)$$

for $B_0 = 10^{-2}$ T, $B_1 = 100\epsilon$ and $m \gtrsim 10^{-17}$ kg. The latter condition on the mass arises because the induced diamagnetic term does not dominate over the NV centre potential. This is due to the small mass and hence small volume of the diamond, which determines the induced diamagnetic potential. For a lighter diamond, if we do not modify the times $\tau_i(\eta)$ and B_1 , the masses would inevitably move through the zero-field region of the magnetic field, and therefore demands a different magnetic field setup, see [35, 36]. Therefore, our analysis holds true for $m \geq 10^{-17}$ kg for $\chi_m \approx -6.2 \times 10^{-9}$ kgm⁻³. Using Eq.13 we can estimate that achieving a superposition size of 20 μm with a 10^{-17} kg mass requires a total time of $\tau_6 \approx 1.25$ s, which corresponds to the moderate magnetic field gradient $\eta \sim 46.8 \text{ Tm}^{-1}$, again using $B_0 = 10^{-2}$ T and $B_1 = 100\epsilon$, which can be achieved in a laboratory [35, 40].

Discussion: Before we conclude, a few comments are in order. In this paper, we have provided a simple mechanism to accelerate heavy neutral masses, with embedded spin, within the SG setup, which can create the spatial superposition $\sim 20 \mu\text{m}$ and for masses, as heavy as 10^{-17} Kg. Our simple scheme fills the gap required for a



(a) Position and velocity for both arms of the interferometer.

(b) Superposition size $\Delta x(t)$ and velocity difference $\Delta v(t)$ with time.

FIG. 4: Figures showing both the actual paths taken through the interferometer, and the superposition size and velocity difference with time. These plots are the result of the combined numerical and analytical analysis. The vertical grey lines represent times $\tau_1 \approx \tau_2$, $\tau_3 \approx \tau_4$, τ_5 and τ_6 . Both figures are for $B_0 = 10^{-2}$ T, $\eta = 46.483$ Tm $^{-1}$ and $m = 10^{-17}$ kg.

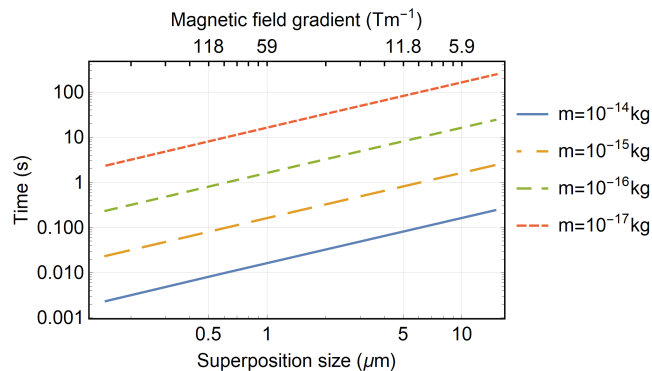


FIG. 5: Superposition size vs. time. This shows the maximal superposition size achievable, as determined by the calculated paths. Note that for masses $m = 10^{-17}$ kg and heavier these results are well approximated by Eq. 13.

realistic “wavefunction splitting” to achieve a large spatial superposition, and herewith opens up new vistas for testing and probing both classical and quantum nature of gravity while also giving access to unprecedented sensing opportunities. It should be noted that some of the SGI durations considered here are beyond what is currently possible, e.g., to place a 10^{-17} kg mass in a $20 \mu\text{m}$ superposition will require ~ 1 sec of spin coherence time. This is beyond what is currently possible and we include such results to provide a roadmap of what may be possible with potential future technological advances. Other major sources of dephasing and decoherence with the masses, duration and superposition size discussed here, have been investigated in Refs [2, 6, 7, 38], in which it was found possible to obtain decoherence rates, due to

background gas scattering and blackbody radiation, well below 10^{-2} Hz, if sufficient cooling is applied. These analyses and constraints will also apply to the present scheme. To conclude, we have presented a roadmap for large spatial superpositions of heavy objects. First realizations should become feasible in the near future as advances are made in several technologies.

Acknowledgements: R. J. M. is supported by a UCL departmental studentship. AM’s research is funded by the Netherlands Organisation for Science and Research (NWO) grant number 680-91-119. R. F. is supported by the Israel Science Foundation.

-
- [1] S. Weinberg, *The Quantum theory of fields. Vol. 1: Foundations* (Cambridge University Press, 2005).
 - [2] S. Bose, A. Mazumdar, G. W. Morley, H. Ulbricht, M. Toroš, M. Paternostro, A. Geraci, P. Barker, M. Kim, and G. Milburn, *Phys. Rev. Lett.* **119**, 240401 (2017), arXiv:1707.06050 [quant-ph].
 - [3] R. J. Marshman, A. Mazumdar, and S. Bose, *Phys. Rev. A* **101**, 052110 (2020).
 - [4] C. Marletto and V. Vedral, *Phys. Rev. Lett.* **119**, 240402 (2017).
 - [5] T. Biswas, E. Gerwick, T. Koivisto, and A. Mazumdar, *Phys. Rev. Lett.* **108**, 031101 (2012), arXiv:1110.5249 [gr-qc].
 - [6] R. J. Marshman, A. Mazumdar, G. W. Morley, P. F. Barker, S. Hoekstra, and S. Bose, *New J. Phys.* **22**, 083012 (2020), arXiv:1807.10830 [gr-qc].
 - [7] T. W. Kamp, R. J. Marshman, S. Bose, and A. Mazumdar, *Phys. Rev. A* **102**, 062807 (2020), arXiv:2006.06931 [quant-ph].
 - [8] M. Arndt, O. Nairz, J. Vos-Andreae, C. Keller, G. van der Zouw, and A. Zeilinger, *Nature* **401**, 680 (1999).

- [9] M. Arndt and K. Hornberger, *Nature Physics* **10**, 271 (2014).
- [10] S. Bose, K. Jacobs, and P. L. Knight, *Physical Review A* **59**, 3204 (1999).
- [11] A. D. Armour, M. P. Blencowe, and K. C. Schwab, *Physical Review Letters* **88**, 148301 (2002).
- [12] W. Marshall, C. Simon, R. Penrose, and D. Bouwmeester, *Physical Review Letters* **91**, 130401 (2003).
- [13] P. Sekatski, M. Aspelmeyer, and N. Sangouard, *Physical Review Letters* **112**, 080502 (2014).
- [14] O. Romero-Isart, M. L. Juan, R. Quidant, and J. I. Cirac, *New Journal of Physics* **12**, 033015 (2010).
- [15] O. Romero-Isart, A. C. Pflanzer, F. Blaser, R. Kaltenbaek, N. Kiesel, M. Aspelmeyer, and J. I. Cirac, *Physical Review Letters* **107**, 020405 (2011).
- [16] F. Khalili, S. Danilishin, H. Miao, H. Müller-Ebhardt, H. Yang, and Y. Chen, *Physical Review Letters* **105**, 070403 (2010).
- [17] M. Scala, M. S. Kim, G. W. Morley, P. F. Barker, and S. Bose, *Physical Review Letters* **111**, 180403 (2013).
- [18] C. Wan, M. Scala, G. W. Morley, A. A. Rahman, H. Ulbricht, J. Bateman, P. F. Barker, S. Bose, and M. S. Kim, *Phys. Rev. Lett.* **117**, 143003 (2016).
- [19] J. Bateman, S. Nimmrichter, K. Hornberger, and H. Ulbricht, "Near-field interferometry of a free-falling nanoparticle from a point-like source," (2014).
- [20] Z. Q. Yin, T. Li, X. Zhang, and L. M. Duan, *Physical Review A* **88**, 033614 (2013).
- [21] H. Pino, J. Prat-Camps, K. Sinha, B. P. Venkatesh, and O. Romero-Isart, *Quantum Science and Technology* **3**, 025001 (2018).
- [22] J. Clarke and M. R. Vanner, *Quantum Science and Technology* **4**, 014003 (2019).
- [23] M. Ringbauer, T. J. Weinhold, L. Howard, A. White, and M. Vanner, *New Journal of Physics* **20**, 053042 (2018).
- [24] K. E. Khosla, M. R. Vanner, N. Ares, and E. A. Laird, *Physical Review X* **8**, 021052 (2018).
- [25] R. Kaltenbaek, G. Hechenblaikner, N. Kiesel, O. Romero-Isart, K. C. Schwab, U. Johann, and M. Aspelmeyer, *Experimental Astronomy* **34**, 123 (2012).
- [26] O. Romero-Isart, *New Journal of Physics* **19**, 123029 (2017).
- [27] J. S. Pedernales, G. W. Morley, and M. B. Plenio, *Physical Review Letters* **125**, 023602 (2020).
- [28] *Atom Optics and Space Physics: Proceedings of the International School of Physics "Enrico Fermi"*.
- [29] Z. Zhou, Y. Margalit, S. Moukouri, Y. Meir, and R. Folman, *Science advances* **6**, eaay8345 (2020).
- [30] A. Al Balushi, W. Cong, and R. B. Mann, *Physical Review A* **98**, 043811 (2018).
- [31] A. Bassi, K. Lochan, S. Satin, T. P. Singh, and H. Ulbricht, *Reviews of Modern Physics* **85**, 471 (2013).
- [32] T. Kovachy, P. Asenbaum, C. Overstreet, C. Donnelly, S. Dickerson, A. Sugarbaker, J. Hogan, and M. Kasevich, *Nature* **528**, 530 (2015).
- [33] J. Murata and S. Tanaka, *Classical and Quantum Gravity* **32**, 033001 (2015).
- [34] C. Wan, *Quantum superposition on nano-mechanical oscillator* (Imperial College London (PhD Thesis), 2017).
- [35] S. Machluf, Y. Japha, and R. Folman, *Nature Communications* **4**, 2424 (2013).
- [36] Y. Margalit, Z. Zhou, O. Dobkowski, Y. Japha, D. Rohrlich, S. Moukouri, and R. Folman, arXiv preprint arXiv:1801.02708 (2018).
- [37] Y. Margalit, Z. Zhou, S. Machluf, Y. Japha, S. Moukouri, and R. Folman, *New Journal of Physics* **21**, 073040 (2019).
- [38] M. Toroš, T. van de Kamp, R. Marshman, M. Kim, A. Mazumdar, and S. Bose, (2020), arXiv:2007.15029 [gr-qc].
- [39] J. H. N. Loubser and J. A. van Wyk, *Reports on Progress in Physics* **41**, 1201 (1978).
- [40] M. Modena, J. Garcia Perez, P. Thonet, C. Petrone, A. Vorozhtsov, O. Dunkel, E. Solodko, and D. Tommasini, in *Conf. Proc.*, Vol. 1205201 (2012) p. TH-PPD010.

Solving the particle dynamics

In this appendix, we provide our analytical and numerical treatment of the equations of motion. The magnetic fields used to create the superposition are

$$\vec{B}(x, y) = (B_0 - \eta x) \hat{x} + \eta y \hat{y} \quad (14)$$

$$\vec{B}(x, y) = B_1 \hat{x} \quad (15)$$

$$\vec{B}(x, y) = -(B_0 - \eta x) \hat{x} - \eta y \hat{y} \quad (16)$$

with the magnetic field being mapped between Eq. 14 to Eq. 15 when $t \in [\tau_1, \tau_2]$, and between Eq. 15 to Eq. 16 when $t \in [\tau_3, \tau_4]$. Figure 6 shows the detail of the experienced magnetic field for each arm of the interferometer during the period in which the magnetic field is modified. This shows that provided the value chosen for B_1 is sufficiently large that the minimum allowable experienced magnetic field ε can be avoided while ensuring a smooth and adiabatic magnetic field transition. When not in this phase ($t \notin [\tau_1, \tau_4]$) the motion is simply governed by the harmonic oscillator potential, whose solution is given by:

$$x(t) = A \cos(\omega t + \phi) + C(s_x) \quad (17)$$

where A and ϕ are determined by the initial conditions, $\omega = \sqrt{-\frac{\chi_m}{\mu_0}} \eta$ is the frequency of the diamagnetic trap and $C(s_x)$ is determined by the spin states and magnetic field (Eqs. 14 and 16). Note that we are always within the adiabatic limit throughout these times, such that $\dot{\omega}/\omega^2 < 1$. We also have

$$C^{s_x=\pm 1} = B_0/\eta \pm \alpha, \quad (18)$$

where $\pm \alpha = -\mu_{\pm} \frac{\mu_0}{\chi_m \eta \bar{\eta}(t)} = -\frac{g e \hbar}{2 m_e} \frac{\mu_0}{\chi_m \eta \bar{\eta}(t)}$.

The trajectory through these times, $t \notin [\tau_1, \tau_4]$, can be constructed by simply assembling the solutions piecewise. To do this, the values of the constants are given by the function of the initial conditions at each time segment. Specifically, if $x(t_0) = x_0$ and $\dot{x}(t_0) = v_0$ serve as the

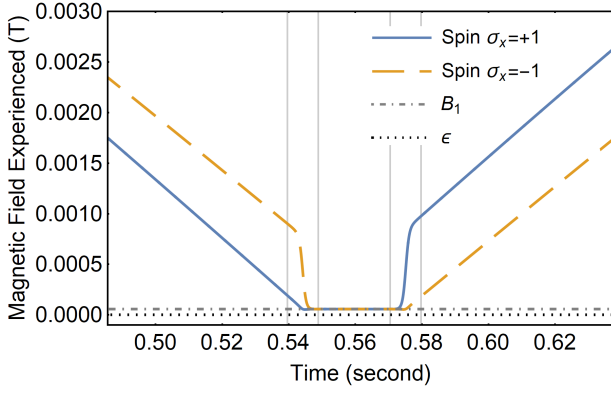


FIG. 6: Magnetic field experienced by each arm of the interferometer with time. The vertical grey lines represent times τ_i for $i = 1, 2, 3, 4$ using $B_0 = 10^{-2}$ T, $\eta = 40$ Tm $^{-1}$ and $B_1 = 100\epsilon$ T.

initial conditions, then

$$A = -(C - x_0) \left(1 + \frac{v_0^2}{\omega^2} (C - x_0)^{-2} \right)^{1/2} \quad (19)$$

$$\phi = \tan^{-1} \left(\frac{v_0}{\omega(C - x_0)} \right) - \omega t_0. \quad (20)$$

For example, if we consider the particle to be initialised in a superposition of spin states $|+1\rangle$ and $|-1\rangle$ at the origin with zero initial velocity, then we can define the initial motion of the two arms as:

$$x_1^+(t) = - \left(\frac{B_0}{\eta} + \alpha \right) \cos(\omega t) + \left(\frac{B_0}{\eta} + \alpha \right) \quad (21)$$

$$x_1^-(t) = - \left(\frac{B_0}{\eta} - \alpha \right) \cos(\omega t) + \left(\frac{B_0}{\eta} - \alpha \right). \quad (22)$$

When the magnetic field is given by Eq. 15 there will be no spin dependant acceleration, that is, there is no force

acting to either create or destroy the spatial superposition. Thus we want to minimise $\tau_4 - \tau_1$. To do this, the initial evolution, $x_1(t)$, should be maintained for as long as possible while still ensuring that Eq.3 is satisfied. Only as the particle approaches the boundary set by Eq.3 is the magnetic field is modified (this marks the time τ_1). Specifically, this is done as the magnetic field experienced by the forward most trajectory approaches B_1 :

$$x_1^+(t \approx \tau_1) = \frac{B_0 - B_1}{\eta}, \quad (23)$$

where we write $x_1^-(\tau_1) = A_1^- \cos(\omega\tau_1) + c_1^-$.

Similarly, the non-zero magnetic field gradient should be returned as soon as possible while ensuring Eq. 3 holds. As such, the magnetic field gradient should begin being restored as the magnetic field experienced by the rearmost trajectory ($x_2^-(t)$) approximately the magnetic field as given by Eq. 16, that is:

$$\begin{aligned} B_1 &= -B_0 + \eta x_2^-(\tau_3) \\ x_2^-(t \approx \tau_3) &= \frac{B_1 - B_0}{\eta} \end{aligned} \quad (24)$$

where x_2^+ and x_2^- are the trajectories when $t \in [\tau_1, \tau_4]$, and are found by numerically integrating the equations of motion.

The final two stages of the trajectories are given by:

$$x_3^+(t) = A_3^+ \cos(\omega t + \phi_3^+) + C_3^+, \quad (25)$$

$$x_3^-(t) = A_3^- \cos(\omega t + \phi_3^-) + C_3^-, \quad (26)$$

$$x_4^+(t) = A_4^+ \cos(\omega t + \phi_4^+) + C_4^+, \quad (27)$$

$$x_4^-(t) = A_4^- \cos(\omega t + \phi_4^-) + C_4^-, \quad (28)$$

where

$$\begin{aligned} A_3^+ &= -(C_3^+ - x_2^+(\tau_2)) \left(1 + \frac{(v_2^+(\tau_2))^2}{\omega^2} (C_3^+ - x_2^+(\tau_2))^{-2} \right)^{1/2}, \\ A_3^- &= -(C_3^- - x_2^-(\tau_2)) \left(1 + \frac{(v_2^-(\tau_2))^2}{\omega^2} (C_3^- - x_2^-(\tau_2))^{-2} \right)^{1/2}, \\ \phi_3^+ &= \tan^{-1} \left(\frac{v_2^+(\tau_2)}{\omega(C_3^+ - x_2^+(\tau_2))} \right) - \omega\tau_2, \\ \phi_3^- &= \tan^{-1} \left(\frac{v_2^-(\tau_2)}{\omega(C_3^- - x_2^-(\tau_2))} \right) - \omega\tau_2, \\ C_3^+ &= - \left(\frac{B_0}{\eta} - \alpha \right), \\ C_3^- &= - \left(\frac{B_0}{\eta} + \alpha \right), \end{aligned} \quad (29)$$

and

$$\begin{aligned}
A_4^+ &= - (C_4^+ - x_3^+(\tau_3)) \left(1 + \frac{(v_3^+(\tau_3))^2}{\omega^2} (C_4^+ - x_3^+(\tau_3))^{-2} \right)^{1/2}, \\
A_4^- &= - (C_4^- - x_3^-(\tau_3)) \left(1 + \frac{(v_3^-(\tau_3))^2}{\omega^2} (C_4^- - x_3^-(\tau_3))^{-2} \right)^{1/2}, \\
\phi_4^+ &= \tan^{-1} \left(\frac{v_3^+(\tau_3)}{\omega(C_4^+ - x_3^+(\tau_3))} \right) - \omega\tau_3, \\
\phi_4^- &= \tan^{-1} \left(\frac{v_3^-(\tau_3)}{\omega(C_4^- - x_3^-(\tau_3))} \right) - \omega\tau_3, \\
C_4^+ &= - \left(\frac{B_0}{\eta} + \alpha \right), \\
C_4^- &= - \left(\frac{B_0}{\eta} - \alpha \right).
\end{aligned} \tag{30}$$

TABLE I: τ_i values used to calculate wave-packet trajectories for example magnetic field gradients (η)

	$\eta = 4 \text{ Tm}^{-1}$	$\eta = 40 \text{ Tm}^{-1}$	$\eta = 400 \text{ Tm}^{-1}$
τ_1	5.39 s	0.534 s	0.0493 s
τ_2	5.39 s	0.539 s	0.0539 s
τ_3	5.80 s	0.580 s	0.0580 s
τ_4	5.80 s	0.584 s	0.0626 s
τ_5	9.01 s	0.902 s	0.0913 s
τ_6	14.8 s	1.48 s	0.148 s

The values for the times τ_5 and τ_6 are fixed by the following conditions:

1. $\Delta x(\tau_6) = x_4^+(\tau_6) - x_4^-(\tau_6) = 0$ and $\Delta v(\tau_6) = v_4^+(\tau_6) - v_4^-(\tau_6) = 0$, such that the two arms of the interferometers are brought together to overlap in both the position and the momentum space, respectively.
2. $x_4^+(\tau_6) > \frac{B_0 + \epsilon}{\eta}$, such that the Majorana spin flip region of the magnetic field is again avoided.

Note that the appropriate time scales which met the above conditions (conditions 1. and 2.) were found *solely* numerically. This has lead to a set of times and the corresponding magnetic field gradients applied during the time period, which we have tabulated in the table I.

There are a couple of points to note here; the time τ_6 , set such that $\Delta v(\tau_6) = 0$ will automatically minimise $\Delta x(\tau_6)$. Also, the value of Δx evaluated at time τ_6 is continuous in τ_5 , and there exists times t_1 and $t_2 \in \mathbb{R}$

such that, when $\tau_5 = t_1$ $\Delta x(\tau_6) > 0$ and when $\tau_5 = t_2$ $\Delta x(\tau_6) < 0$. In a nut-shell the procedure to find the correct values of τ_5 and τ_6 are:

1. to make an initial guess for the value of τ_5 which was used to calculate a complete trajectory, typically this is $\tau_5 = 2\tau_4$.
2. From this we have evaluated the value of τ_6 , which we have determined using the relation $\Delta v(\tau_6) = 0$, and
3. the corresponding value of $\Delta x(\tau_6)$ was then evaluated. This allows the the assumed value for τ_5 to be optimised accordingly. Specifically noting that increasing τ_5 will lead to decrease the value of $\Delta x(\tau_6)$.

It is perhaps worth pointing out that we are not modelling the background laser field interacting with the particle. Therefore, the particle energy appears here to be *not* conserved at τ_5 when the microwave pulse impinges upon the particle to flip the internal spin to align or anti-align with the bias magnetic field. When this spin-flip occurs, the state's potential energy is modified, and here we treat the process as instantaneous, while considering the laser pulse as part of a reservoir. Nevertheless, this affects our SG-setup, which should be treated as a part of an open system. Finally, the centre of a mass movement, which causes the interferometer's lopsided appearance, can be understood due to the diamagnetic effect dominating over the NV-centre induced, spin-dependent accelerations.